Cement and Concrete Research 163 (2023) 107031

Contents lists available at ScienceDirect

Cement and Concrete Research

journal homepage: www.elsevier.com/locate/cemconres

On mesoscale modeling of concrete: Role of heterogeneities on local stresses, strains, and representative volume element

Mohmad M. Thakur [a], N. Axel Henningsson [b], Jonas Engqvist [b], Pierre-Olivier Autran [c], Jonathan P. Wright [c], Ryan C. Hurley [a,d,e,*]

[a] Hopkins Extreme Materials Institute, Johns Hopkins University, Baltimore, MD 21218, USA
[b] Division of Solid Mechanics, Lund University, Box 118, 221 00 Lund, Sweden
[c] ESRF-The European Synchrotron, 71 Avenue des Martyrs, 38000 Grenoble, France
[d] Department of Mechanical Engineering, Johns Hopkins University, Baltimore, MD 21218, USA
[e] Department of Civil and Systems Engineering, Johns Hopkins University, Baltimore, MD 21218, USA

ARTICLE INFO

Keywords:
Concrete
Mesoscale modeling
Experiments
X-ray tomography
3D X-ray diffraction
Heterogeneity
Representative volume element

ABSTRACT

The mechanics of concrete can be understood comprehensively only if its heterogeneous microstructure is considered in experiments and simulations. We combine mesoscale modeling, in-situ X-ray computed tomography imaging, and in-situ 3D X-ray diffraction measurements for one of the first times to investigate the role of heterogeneities on macroscopic and microscopic responses in concrete. The focus here is on heterogeneities at the micron scale: aggregates, cement paste, interfacial transition zone, high-density phases, and voids. We specifically seek to answer whether all levels of heterogeneities are essential in predicting: (a) elastic macroscopic stress–strain response, (b) microscopic elastic stress–strain concentrations, and (c) representative volume element size for elastic responses. The results demonstrate the significant influence of heterogeneities on local strains in matrix phases and the minimal influence of heterogenities on stresses in individual grains.

1. Introduction

Concrete is a complex engineering material, widely used in the construction industry. At the macroscale, concrete appears as a two-phase material consisting of aggregates and mortar. However, at smaller scales, imaging techniques such as scanning electron microscopy and X-ray computed tomography (XRCT) reveal concrete as a multi-phase material with heterogeneous microstructure [1,2]. A comprehensive understanding of the underlying mechanics with due consideration to the microstructural heterogeneity is essential to better engineer next-generation composite materials such as concrete.

The elastic contrast exhibited by individual phases in concrete has been quantified to some extent using nanoindentation [3–5]. Some of the earliest nanoindentation studies identified two phases in a cement mortar: low-density C–S–H and high-density C–S–H, characterized by low elastic stiffness and high elastic stiffness, respectively [5,6]. The statistical analysis of the nanoindentation data and coupling of nanoindentation with scanning electron microscopy and energy dispersive spectroscopy independently characterized elastic properties of additional phases in concrete such as clinker, portlandite (CH), and ultra-high density C–S–H [7–10]. Further, Mondal et al. [11] estimated the modulus of the interfacial transition zone (ITZ) as approximately 0.8 times the modulus of the cement paste matrix. These experimental developments confirmed structural heterogeneity in concrete with distinct material properties and provided the much-needed impetus to the research on advanced micromechanics-based continuum models [12–14] and mesoscale numerical models [15–18].

Mesoscale modeling incorporates a 3D representation of a microstructure in numerical modeling — a powerful approach to explore the role of heterogeneities on the mechanical response [19–21]. Mesoscale modeling frameworks consist of two main ingredients: (a) capturing material microstructure realistically, typically at a micron scale, using XRCT imaging or virtual specimen generation algorithms, and (b) solving boundary value problems on the material microstructure using appropriate numerical method. The heterogeneities in concrete exhibit multiple length scales [22,23]. Incorporating all the scales of heterogeneity in a single modeling framework is challenging and can be impractical. Most of the mesoscale studies assumed concrete as a two-phase or three-phase material, consisting of aggregates, matrix, and ITZ as an interface element [20,24–26]. The studies that include additional levels of the heterogeneities in mesoscale modeling

* Corresponding author at: Hopkins Extreme Materials Institute, Johns Hopkins University, Baltimore, MD 21218, USA.
E-mail addresses: mthakur3@jh.edu (M.M. Thakur), rhurley6@jhu.edu (R.C. Hurley).

https://doi.org/10.1016/j.cemconres.2022.107031
Received 26 August 2022; Received in revised form 20 October 2022; Accepted 4 November 2022
Available online 24 November 2022

Nomenclature

Abbreviations

APV	Aggregate, Paste, Voids
$APVH$	Aggregate, Paste, Voids, High-Density Phase
$APVI$	Aggregate, Paste, Voids, ITZ
$APVIH-NS$	Aggregate, Paste, Voids, ITZ, High-Density Phase, Non Stochastic
$APVIH$	Aggregate, Paste, Voids, ITZ, High-Density Phase
$S1$	Sample S1 with target aggregate volume fraction equal to 20%
$S2$	Sample S1 with target aggregate volume fraction equal to 30%

of concrete are rare, but not completely missing in the literature. Gao et al. [16] considered four phases in mesoscale modeling of cement paste: C–S–H, portlandite, clinker, and pores. They investigated the role of structural heterogeneity on the elastic modulus of the cement paste and provided an empirical equation to predict the modulus of cement paste. Homel et al. [15] conducted a comprehensive mesoscale investigation of damage progression in ultra-high performance concrete. They combined XRCT imaging, SEM, EDS, cement hydration modeling, and nanoindentation to incorporate the influence of structural heterogeneity in mesoscale modeling and concluded structural heterogeneity was necessary to predict complex failure propagation in concrete.

Despite the high-quality investigations referenced above, the role of structural heterogeneities on the mechanical response of the concrete remains largely elusive. The following key questions remain still unanswered and deserve urgent attention:

1. What are the levels of heterogeneities that should be considered in mesoscale modeling of concrete in determining a specific property of interest or in exploring mechanisms relevant to specific physics of a boundary value problem? Are all the heterogeneities equally important?
2. How do stress and strain localize with different levels of heterogeneities? How sensitive are these heterogeneities to the material contrast and aggregate volume fraction?
3. To what detail are mesoscale models calibrated with high-quality experiments?
4. How does the minimum representative volume element size change as a function of heterogeneity in mesoscale modeling of concrete?

Our work seeks to shed light on these important questions on heterogeneities in concrete and their influence on stress–strain concentrations. Mesoscale models require rigorous validation with experiments — beyond macroscopic stress–strain response, possibly by considering local stresses in individual sand grains. In the present work, we calibrate our mesoscale models, both at the macroscopic scale and microscale, by comparing simulations with in-situ image-based experiments using XRCT and 3D X-ray diffraction (3DXRD) techniques. 3DXRD quantifies stresses in individual crystalline aggregates and we use these measurements to calibrate our mesoscale simulations at the microscale. Furthermore, we include a stochastic description of material properties for different phases in mesoscale simulations and compare a few of these simulations with those using a deterministic description of material properties. It is important to note here that the heterogeneities in concrete below the micron scale are not considered in the present work. It is essential to answer the questions raised in this section to enhance a fundamental understanding of the material response with prolific implications in tailoring the microstructure of concrete composites to generate new materials of superior performance and for future mesoscale simulations in concrete. For brevity and focus, we consider only the elastic response in this paper and delay the consideration of damage and inelasticity for future work.

2. Materials and methods

This section describes experiments, data analysis, and numerical modeling performed in this work to explore the role of heterogeneities on stresses and strains in concrete.

2.1. Sample preparation

The concrete samples were prepared using ordinary portland cement (OPC), single crystal quartz aggregates, and tap water. Single crystal quartz aggregates are well suited for 3DXRD and are chemically similar to Ottawa sand. Single crystal quartz grains were obtained by ball milling a block of quartz (Sawyer Technical Materials, LLC) for 30 s using a stainless steel ball mill and stainless-steel vial (SPEX SamplePrep Mixer/Mill 8000D ball mill). The ball milled grains were air milled in a stainless steel chamber for half an hour with stainless steel balls at 20 psi pressure. The air-milled grains were then sieved to retain the grains between 107 μm and 125 μm for concrete preparation. Two samples were prepared, referred to as S1 and S2 here onwards, with the target aggregate volume fraction equal to 20% and 30%, respectively. Cement and aggregates were mixed in a small weigh boat in the appropriate quantity needed to obtain the target aggregate volume fraction. Tap water was then added to the cement-aggregate mixture with a water-to-cement ratio equal to 0.5 by weight. It was observed that Sample S2, consisting of a higher volume fraction of aggregates, produced less workable concrete compared to Sample S1. This may have happened because the large number of aggregates in Sample S2 absorbed more water compared to Sample S1. It may also have happened because of an uneven distribution of water content throughout the slurry prepared prior to casting Sample S2 — not all of the slurry was cast into the mold. This is expected to produce mortar of different elastic properties in Sample S1 and Sample S2 as the actual water-to-cement ratio in sample S2 was lower. We will come back to this point again in Section 2.5, where we discuss the calibration of material properties for the two samples. The fresh concrete was poured into a cylindrical polymer membrane and placed on a steel pin to obtain a cylindrical specimen of height and diameter equal to 2 mm. The choice for the size of the sample was limited by XRCT and 3DXRD but was large enough to provide representative measurements. The specimen was compacted by tamping and vibrating at a 200 Hz frequency for 30 s and was then covered in a small Ziploc bag for 24 h to prevent loss of moisture. After 24 h, a saturated solution of lime was poured into the Ziploc bag containing the specimen for 28 days. After 28 days, the samples were taken out of saturated lime solution and allowed to air dry at room temperature. The ends of the cylindrical samples were smoothened with high grit sandpaper and stored for experiments at an approximate age of 60 days. It should be noted that only fine aggregates were in this work.

2.2. Experiments and in-situ X-ray imaging

Experiments were performed at the ID11 beamline of the European Synchrotron Radiation Facility (ESRF) in Grenoble, France. Each sample was first removed from the cylindrical polymer membrane in which it was cast and subsequently inserted into a new, thin polymer membrane intended to align the sample with compressing pins and capture sample fragments during fracture, but not to provide lateral support to the sample during compression. A steel hemisphere of approximately the same diameter as each sample was placed on top of each sample to provide uniform vertical traction during mechanical compression. Samples were then placed on a 1.5 mm diameter steel pin located in

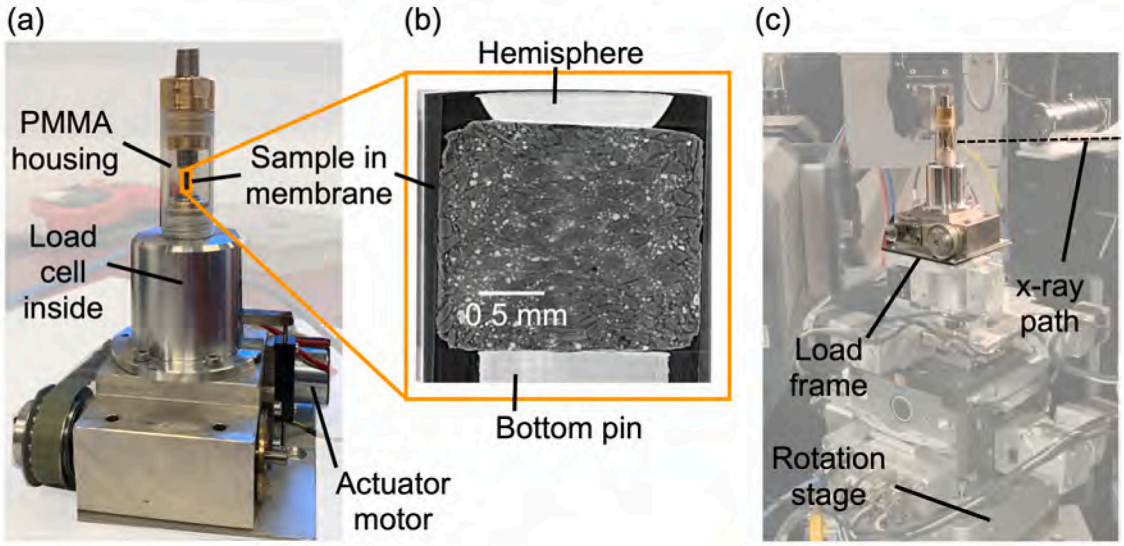

Fig. 1. (a) The load frame with a sample inserted. (b) A view of the sample confined between a bottom pin, a top hemisphere, and a membrane. (c) The load frame mounted on the rotation stage at the ESRF beamline ID11.

a custom uniaxial compression frame similar to one described in prior work [27]. A steel pin attached to the top of the compression frame was brought into the top of the membrane as the frame was sealed. Fig. 1(a) shows the frame with a sample placed between the compressing pins. A critical feature of the compression frame is the polymethyl methacrylate (PMMA) housing which provides 360° X-ray transparency for measurements. Fig. 1(b) shows a vertical slice through the XRCT image of sample S2, illustrating the confinement of the sample between a bottom pin, a hemisphere, and a membrane. After each sample was placed in the frame, the frame was mounted onto a rotation stage and into the X-ray beam path in the ID11 hutch, as shown in Fig. 1(c). Experiments proceeded by incrementally advancing the actuator that pushes the bottom pin upward to compress the sample and hemisphere into the top pin, which remained static. Increments were chosen to impose small strain (less than 0.04) or compressive load (less than 20 N) changes. Experiments proceeded until noticeable sample failure (i.e., a significant load drop or the appearance of fractures within samples) or until about 0.3% strain was reached. Between each increment of loading, sample strain was held constant and samples were rotated 360° twice, once for XRCT and once for 3DXRD measurements. XRCT measurements were made while the sample was illuminated by an X-ray box beam with monochromatic energy of 41.6 keV and dimensions of 2.4 mm × 2.4 mm. XRCT measurements were made by recording 6144 radiographs on an imaging camera with a 1.2 mm ×1.2 mm field of view while the sample rotated 360°. A half-acquisition technique was used to record radiographs and perform reconstructions because samples were wider than the 1.2 mm wide field of view. In the half-acquisition technique, half of the sample was visible in the first radiograph captured during rotation, and the sample processed about a vertical axis to bring the other half of the sample fully into the radiograph in the 3072nd radiograph. Reconstructions were performed in the reconstruction software Nabu [28] and exploited phase contrast. Reconstructed images had a native resolution of 0.63 μm/pixel. 3DXRD measurements were made by recording 3600 diffraction patterns on a FreLoN area detector situated approximately 1.2 m downstream of the sample while the full sample was illuminated by the 41.6 keV monochromatic X-ray beam. 3DXRD analysis was performed in ImageD11 [29], as described in our previous work [27], and yielded the positions, orientations, and strain tensors of each single-crystal quartz grain in the samples with resolutions of approximately 10 μm, 0.05°, and 5×10^{-5} to 1×10^{-4}, respectively [30,31]. The orientation and the elastic strain tensor of each grain was used along with the anisotropic elastic stiffness of quartz [32] to calculate the elastic stress tensor of each grain [30,31].

2.3. Digital volume correlation (DVC)

Digital volume correlation was performed using the open-source software SPAM [33] to calculate displacement and strain fields from XRCT images obtained at different increments of sample strain. XRCT images were downsampled by a factor of 4 to decrease the computational time for DVC calculations which resulted in an effective pixel resolution of 2.52 μm/pixel. DVC calculations proceeded by first performing a full-image registration between the XRCT image obtained for each sample prior to mechanical loading and each subsequent XRCT image. Each XRCT image of the *entire sample* was then tessellated into cubic correlation windows within which a classical Lucas and Kanade approach was used to calculate displacement and rotation, using the full-image registration as an initial guess [34]. The speckle pattern employed by the DVC algorithm was the natural heterogeneity of the cement paste observable in XRCT images. Correlation windows overlapping inclusions and voids, which do not feature such a speckle, were later excluded from the analysis. The correlation window size was chosen to be 40 voxels, approximately 6 times the average feature size of the speckle obtained from an auto-correlation calculation, which falls within 3–6 times the average feature size range recommended by typical DVC texts [35]. From displacements and rotations obtained in each correlation window, a linearized strain tensor was obtained through numerical differentiation and interpolated across the entirety of the sample to provide a full strain field. This procedure yielded a reliable strain field throughout the majority of the sample. However, the half-acquisition and reconstruction technique introduced an artifact close to the rotation axis of the sample that likely arose from minute shifts in the true rotation center from that assumed by the reconstruction software. In particular, half-acquisition and reconstruction require stitching radiographs from one viewing angle of the sample, θ, and from viewing angle $\theta+180°$, such that the stitched radiographs used in reconstruction feature the entire width of the sample. Random, unrepeatable tilt, displacement, or rotation angle deviations of the sample in sequential XRCT scans introduce artificial strains through DVC. These strains are sub-pixel in nature but still of a greater magnitude than the strains of interest in cement paste. Therefore, strains computed from displacements obtained in correlation windows belonging to the regions in which radiographs were stitched (e.g., near the rotation axis) are ignored in our analysis. The resulting strains from DVC located away from the rotation axis were primarily used in this study to calculate a macroscopic sample strain, ϵ_{zz}, to impose on the mesoscale model, as described in Section 3.1.

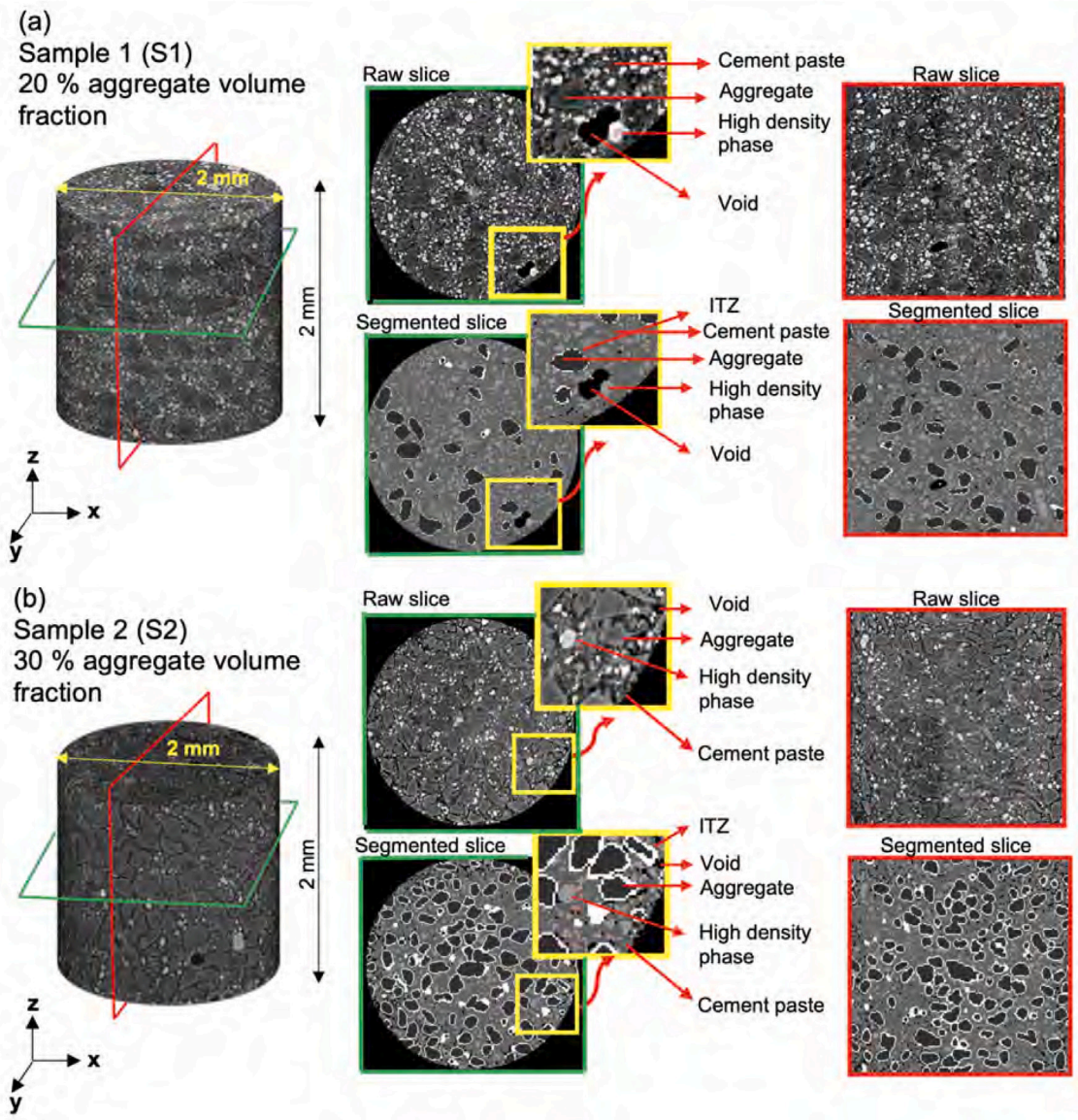

Fig. 2. (a) XRCT image of sample 1 (S1). (b) XRCT image of sample 2 (S2).

2.4. Mesoscale microstructure to finite element discretization

The reconstructed data from XRCT imaging needs to be processed to segment the data into individual phases. The image processing and segmentation were performed in Matlab. The raw and segmented images for two concrete specimens used in the present work are shown in Fig. 2. The images were smoothed by applying an anisotropic diffusion filter [36] before carrying out segmentation. The segmentation of XRCT images of concrete to different phases is straightforward, except for segmenting aggregates from the cement paste, as the X-ray attenuation of the aggregates and the cement paste is similar. The attenuation contrast allows the segmentation of air voids, high-density phases, and cement paste plus aggregates as a single phase. The cement paste and the aggregates were segmented by a standard deviation-based threshold which relies on the fact that the gray-scale values belonging to the aggregate volume are homogeneous compared to the gray-scale values belonging to the mortar. The standard deviation threshold is carried out by computing the standard deviation of gray-scale values in cubic windows, followed by the segmentation of aggregates from cement paste by selecting a suitable standard deviation threshold. The size of the cubic window should be large enough to capture the high and low standard deviation regions but as small as possible to capture the small aggregates. The standard deviation-based segmentation in concrete has been discussed in detail in [37] and implemented in prior work by the last author [38]. In the present work, a cubic window size of 9 voxels, approximately 22.7 μm, was selected to calculate the standard deviation map. The size of the selected cubic window was much smaller than the size of the aggregates (107 μm to 125 μm). The standard deviation threshold value equal to 3000 resulted in reasonably accurate segmentation of aggregates based on visual inspection. Prior work has employed standard deviation based identification for aggregates in XRCT images of concrete [37,38] and also noted reliability of the method by comparison to known volume fractions, visual inspection of images, or to volumetric images obtained from neutron tomography. However, we acknowledge that the standard deviation based aggregate identification may modify aggregate morphology or result in different aggregate volume fractions than truly present. More systematic research is needed to understand the limitations of the method.

ITZ cannot be directly identified in XRCT images but is considered a critical link in micro-mechanics studies. In prior mesoscale simulations, ITZ was either modeled as an interface element of zero thickness [26] or by considering unrealistically large size ITZ with a size larger than

Table 1
Volume fraction of different phases of sample S1 and sample S2 obtained after segmentation of XRCT images.

Phase	Aggregate	Cement paste	ITZ	Void	High density phase
S1	0.195	0.581	0.102	0.002	0.120
S2	0.253	0.474	0.140	0.04	0.093

100 μm [20]. In the present work, we assigned 4 voxels, approximately 10 μm, around each aggregate surface as ITZ based on the findings from literature [39,40]. We considered only one size of ITZ in our mesoscale simulations. Previous work suggests that changes in ITZ size in mesoscale simulations has a minimal effect on mechanical response, especially in the elastic regime of material behavior [20]. In fact, changes in ITZ thickness from 0.1 to 0.8 mm in prior work indicated a negligible effect on elastic stiffness and a minor effect on the tensile strength and strain to damage [20].

The volume fraction of different phases obtained after segmentation is summarized in Table 1. It can be observed that the computed aggregate volume fraction in Sample S2, 0.253, is different than target aggregate volume fraction of 0.3. We believe that the difference in observed and target aggregate volume fraction is primarily due to casting Sample S2 using only a portion of the slurry mixed with aggregates at the target volume fraction. We also acknowledge that the standard deviation based aggregate identification may result in deviations from measured and true aggregate volume fractions, but we believe this to be a secondary factor in the discrepancy.

Next, we discretize the segmented XRCT images directly to the finite element mesh. The structural heterogeneity in concrete results in the complex microstructure. The generation of the robust finite element meshes directly from images that conform to different phases in concrete can be challenging. This problem is partly resolved in prior studies by considering only two phases in concrete for numerical simulations — mortar and aggregate. However, homogenization of the cement paste into a single-phase fails to capture local stresses and strains accurately. A more robust mesoscale description of concrete requires additional phases that manifest additional structural and material heterogeneity. The different phases in concrete that were identified from CT images in the preceding sub-section are aggregates, cement paste, high-density phase, and air voids. ITZ was indirectly incorporated by assigning a 10 μm thick layer as ITZ around each aggregate surface.

The size of the phases in concrete can vary significantly, for instance, the dimensions of the aggregates and ITZ, for the concrete specimens considered in this study are 115 μm and 10 μm, respectively. This is an essential consideration for finite element discretization as selecting a uniform fine mesh size can result in a large number of elements which makes simulations, pre-processing, and post-processing of the results computationally expensive. On the other hand uniform, coarse mesh size fails to capture small microstructural features. Therefore, a customized option for mesh refinement is necessary to include different levels of heterogeneities of concrete.

Simpleware software (https://www.synopsys.com/simpleware.html) provides an option to discretize 3D images to a finite element mesh. The software offers different levels of mesh refinement for different parts/phases. Furthermore, the gradient-based mesh can also be adopted within a single phase. This is particularly useful for concrete as higher mesh density is required at surfaces of different phases compared to the bulk of the phases, e.g., the surface of the aggregate requires high mesh density compared to the inner core of the aggregate to capture stress and strain concentrations precisely. Also, both linear and quadratic element types are available to the user for mesh discretization. Fig. 3 shows finite element mesh generated for a concrete sample using Simpleware. We further down-sampled XRCT images during mesh generation to an effective resolution of 10 μm/pixel. A zoomed-in view clearly shows different levels of mesh refinement in different phases. The mesh generated in Simpleware can be imported to the finite element software package Abaqus. In the present work, approximately 18 million and 25 million linear tetrahedral elements were used to discretize sample 1 (20% aggregate volume fraction) and sample 2 (30% aggregate volume fraction), respectively. A preliminary finite element study on sample 1 with quadratic tetrahedral elements failed to progress due to insufficient RAM on a computing workstation with 192 GB RAM. In addition, mesh sensitivity was not considered in present study. The use of quadrilateral elements and increasing the number of elements used to discretize ITZ layer is recommended in future studies to provide better stress estimation within the ITZ, but is beyond the scope of this work.

2.5. Mesoscale finite element simulations

The finite element mesh obtained directly from XRCT images was imported to the commercial FEM solver Abaqus. The linear elastic constitutive model was assumed for individual phases, an advantage offered by mesoscale simulations to bypass the complex phenomenological constitutive models, and in addition, material damage was not considered in our simulations. We consider different phases in mesoscale simulations: Cement paste (C–S–H), aggregates, ITZ, high-density phases (portlandite (CH)+clinker), and capillary porosity for two concrete samples S1 and S2. Different levels of heterogeneities in this study are summarized below and schematically shown in Fig. 4 to explore the influence of different levels of heterogeneities on macro and microscale response:

1. Aggregates, cement paste (C–S–H), air voids — denoted as APV
2. Aggregates, cement paste (C–S–H), air voids, ITZ — denoted as APVI
3. Aggregates, cement paste (C–S–H), air voids, high-density phase — denoted as APVH
4. Aggregates, cement paste (C–S–H), air voids, ITZ, high-density phase — denoted as APVIH

The material properties of the grains are known a priori as the grains were milled from single crystal quartz blocks. The elastic properties of single crystal quartz are reported in [32] and the mean value of the elastic modulus in different directions was used as the elastic modulus for grains. The stochastic material properties are incorporated for different phases in the matrix for samples S1 and S2 for the four heterogeneity levels described above. For the heterogeneity level APVIH, deterministic material properties were incorporated to compare the response obtained from stochastic and non-stochastic material properties. The evidence from nano-indentation experiments in literature reveals variance in material properties of individual phases. The material parameters for different phases used in simulations are summarized in Table 2. The parameters for cement paste and high-density phase were selected based on values reported in the literature with some modifications based on preliminary calibration [8,10,22,41]. The modulus of the ITZ was assumed to be equal to 0.8 times the modulus of cement paste [11]. The material parameters were calibrated with experimental results based on macroscale stress–strain response and microscale stresses in individual grains. Only mean values of the elastic modulus for different phases reported in Table 2 were considered for simulations with deterministic material models. For simulations considering stochastic material models, the elastic modulus was assigned randomly to the sample: 50% of each phase was assigned mean values, 25% was assigned mean plus one standard deviation and the remaining 25% was assigned mean minus one standard deviation. This approach of assigning stochastic material properties is rather simplistic and does not capture the detailed stochasticity in material properties that exists in the concrete. Incorporating realistic stochasticity requires additional material characterization, preferably captured by conducting statistical nanoindentation experiments.

Furthermore, it should be noted that the material parameters selected for the cement paste are different for the two samples because

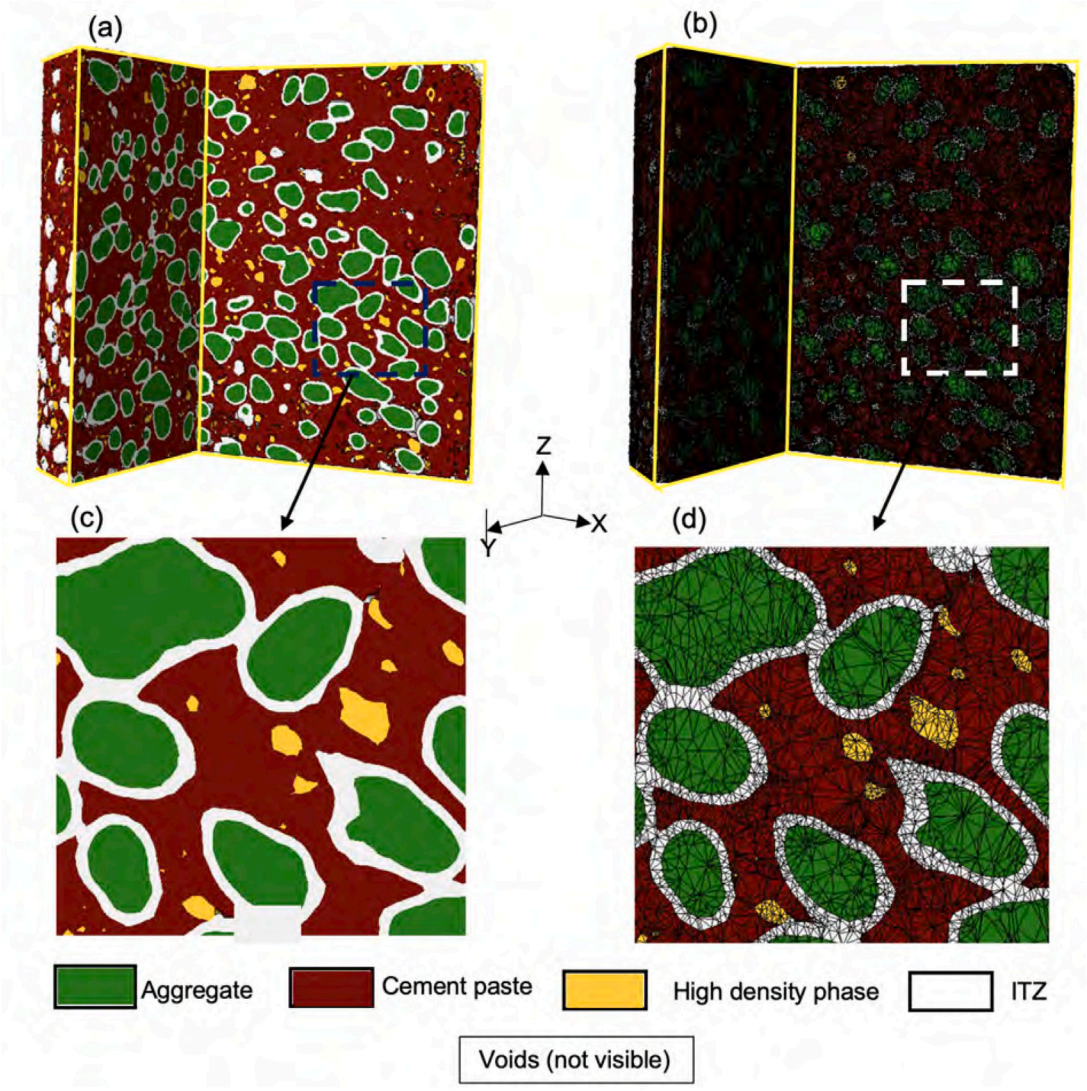

Fig. 3. XRCT image to finite element discretization of sample S2. The image of sample S1 is not shown here for brevity. (a) XRCT image. (b) Meshed XRCT image. (c) Zoomed-in region of XRCT image. (d) Zoomed-in region of meshed XRCT image.

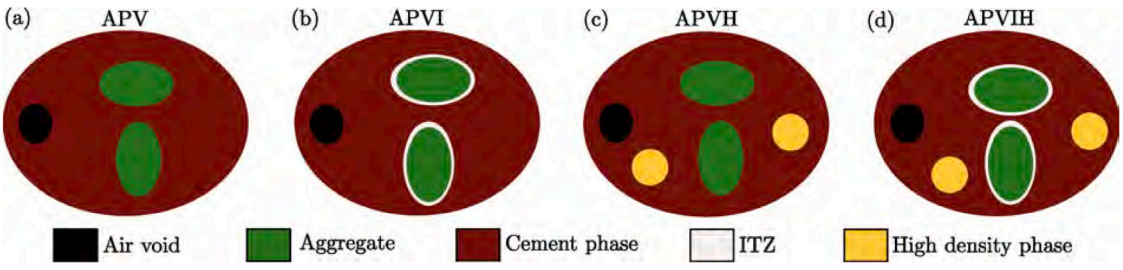

Fig. 4. Schematic representation of different levels of heterogeneities considered in this study. (a) APV: Aggregate, Cement paste, Voids. (b) APVI: Aggregate, Cement paste, Voids, ITZ. (c) APVH: Aggregate, Cement paste, Voids, High-density phase. (d) APVIH: Aggregate, Cement paste, Voids, ITZ, High-density phase.

of the different water–cement ratios in Sample S1 and Sample S2, as discussed in Section 2.1. Cho et al. [42] observed that the elastic modulus of mortar increased significantly as the water–cement ratio decreased. The increase in elastic modulus of mortar is particularly high at low water–cement ratios. Another factor that could influence calibration is the uncertainties in the identified phase fractions of aggregates and mortar. It is possible that certain aggregates, especially elongated grains, may be assigned to mortar rather than aggregate in a standard deviation-based thresholding segmentation procedure. We acknowledge these uncertainties in our work, particularly due to the challenges in preparing highly repeatable concrete samples at small scales.

The sample was loaded in a uniaxial compression stress path similar to experiments by applying vertical displacement at the top and

Table 2
Material properties used for different phases in mesoscale simulations for sample S1 and sample S2.

Phase	Sample (S1)		Sample (S2)	
	E (GPa)	ν	E (GPa)	ν
Aggregate	87.2	0.12	87.2	0.12
Cement paste	10 ± 4.7	0.23	20 ± 4.7	0.23
ITZ	8 ± 5.3	0.23	16 ± 5.3	0.23
High density phase	40 ± 5.2	0.24	40 ± 5.2	0.24
Air void	0	0	0	0

restraining vertical displacement at the bottom. The platens were not directly incorporated in simulations to avoid modeling contact non-linearity due to the high computational cost. The eccentricities in loading were observed in experiments due to some misalignment in platens. These eccentricities were incorporated in simulations by applying displacement boundary conditions only to the regions of the sample that were in contact with platens. Furthermore, the influence of horizontal restraint imposed due to the friction between platens and sample was indirectly checked by carrying out two simulations on Sample S1 — the first one by imposing zero horizontal displacements on the top and bottom regions of the sample to replicate the frictional boundary, the second one with free to move horizontal displacement boundary condition on top and bottom regions of the sample to replicate to the lubricated boundary. We did not observe a significant difference in the two simulations and decided to restrain the top and bottom regions in horizontal directions in the rest of the simulations. However, we acknowledge that the frictional and lubricated boundary can influence failure patterns, but in the present work, we focus on stress and strain concentrations in the elastic regime, much before the cracking or damage in the material.

2.6. Representative volume element

The concept of Representative Volume Element (RVE) is essential in the mechanics of heterogeneous materials for the reliable prediction of effective material properties. Prior work established the size of the RVE to be dependent on the property of interest, material contrast, volume fraction and boundary conditions [43–45]. Here, we focus on investigating the influence of heterogeneity on RVE sizes in concrete for samples with different aggregate volume fractions. In addition, we examine the dependence of RVE size on phase volume fractions and components of the stress tensor. RVE size is determined based on the evolution of the variance of a property with the increase in size and can be described according to the power law expressed in Eq. (1), where z is a property of interest, v is sampling volume or size, A is a material constant and b indicates the rate of reduction in variance with the increase in sampling size. Prior studies demonstrated that the value of b transitions from less than 1 to greater than 1 as sampling volume increases to transition from statistically heterogeneous to statistically homogeneous media [46,47]

$$var(z(v)) = A/v^b \tag{1}$$

XRCT images and mesoscale finite element simulations are used here to predict RVE sizes. The effect of the boundary is eliminated by considering a cube sufficiently inside the cylinder as a domain of interest. A sampling size is chosen and non-overlapping cubical windows of side length equal to the sampling size are tessellated over the domain of interest as shown in Fig. 5. The variance of a physical quantity is determined for non-overlapping cubical windows of the same size. The procedure is repeated for the range of sampling sizes to obtain a plot of variance and sampling size/volume, also known as a variogram, as shown in Fig. 5(b). In the present work, variance is transformed into the dimensionless coefficient of variation which is defined as the ratio of the standard deviation to the mean of a physical quantity. It is essential to obtain the transition from $b < 1$ to $b > 1$ in variogram to predict the RVE size. It is sufficient to determine the RVE size from the slope of a variogram for a region with $b > 1$ as shown in Fig. 5(b). RVE size should be associated with the precision of a property, in this work, a coefficient of variation equal to 0.1 was chosen to determine the RVE size.

3. Results and discussion

3.1. Macroscale response

The macroscale response obtained from experiments and mesoscale simulations is presented here for two concrete samples, S1 and S2, consisting of aggregate volume fractions equal to 0.195 and 0.253, respectively. The average stress in the loading direction (σ_{zz}) for experiments was obtained by dividing the force measured from the load cell by the area of the sample. The strain in the loading direction (ϵ_{zz}) for experiments was obtained by averaging the strains of the correlation windows obtained by performing DVC on in-situ XRCT images. The strains in some of the correlation windows were tensile and such values were ignored for obtaining the average ϵ_{zz} due to possible errors caused by half acquisition XRCT imaging. Small tensile strains in the loading direction may exist due to the complex microstructure of concrete; however, such tensile strains may exist, if at all, only locally at a scale much smaller than the size of the correlation window chosen in this work (≈100 μm). The validity of this assumption was confirmed from mesoscale simulations by obtaining ϵ_{zz} in sub-volumes with a size equal to 100 μm. The ϵ_{zz} distribution at this length scale did not indicate the presence of any tensile stains. The ϵ_{zz} obtained from DVC is more representative of the strains experienced by the sample compared to the strain obtained from single-point measurement devices such as LVDT, where results are affected by local crushing at the sample-platen interface. The average stresses in the grain phase were obtained by averaging the stresses in individual grains measured using 3DXRD. The components of the stress and strain tensor from the mesoscale simulations were obtained as the volume-weighted averaged quantities, as shown in Eqs. (2) and (3). $(\hat{\sigma}_{ij})_n$ represents the stress component at an integration point of a finite element, v_n represents the volume of a finite element, σ_{ij} represents the volume averaged stress and V represents the volume under consideration. The symbols have a similar meaning in Eq. (3) with the use of strain instead of stress.

$$\sigma_{ij} = \frac{1}{V}\int_V \hat{\sigma}_{ij}\, dv = \frac{1}{V}\sum_{n=1}^{nelements} (\hat{\sigma}_{ij})_n v_n. \tag{2}$$

$$\epsilon_{ij} = \frac{1}{V}\int_V \hat{\epsilon}_{ij}\, dv = \frac{1}{V}\sum_{n=1}^{nelements} (\hat{\epsilon}_{ij})_n v_n. \tag{3}$$

Fig. 6(a) and (b) show the average stress and average strain in the loading direction in samples S1 and S2 from experiments and simulations. Fig. 6(c) and (d) shows the average stress in the grain phase and average strain in the whole sample in the loading direction in samples S1 and S2 from experiments and simulations. Sample S2 exhibits yielding, approximately at 0.18% axial strain, which is not captured by the mesoscale modeling, as the scope of this work was to investigate stress and strain concentrations in an elastic regime only. The two important findings that emerge from the results shown in Fig. 6 are as follows. (i) Qualitatively, the experiments and numerical simulations show a promising match for both the samples, S1 and S2. Besides the average stress–strain response, the average stress in the grain phase also matches reasonably well for experiments and simulations. (ii) The influence of different levels of heterogeneity in mesoscale simulations on average stress–strain response and average stresses in the grain phase is marginal. The influence of different levels of heterogeneity on the modulus of elasticity is summarized in Table 3.

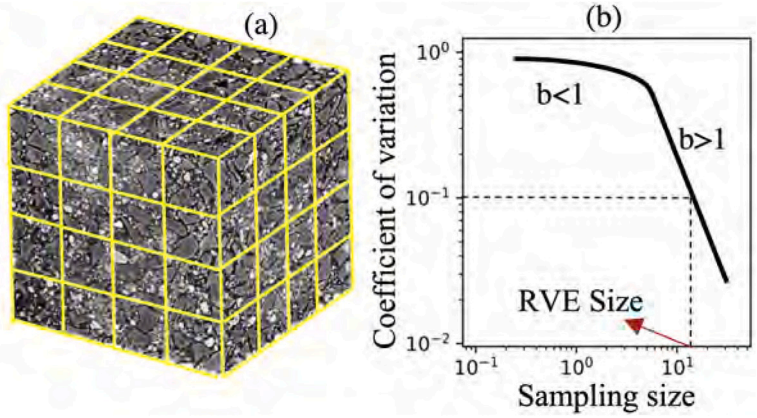

Fig. 5. RVE prediction in concrete. (a) Non-overlapping cubical windows of the same size tessellating a region of interest. (b) Variogram to predict RVE size.

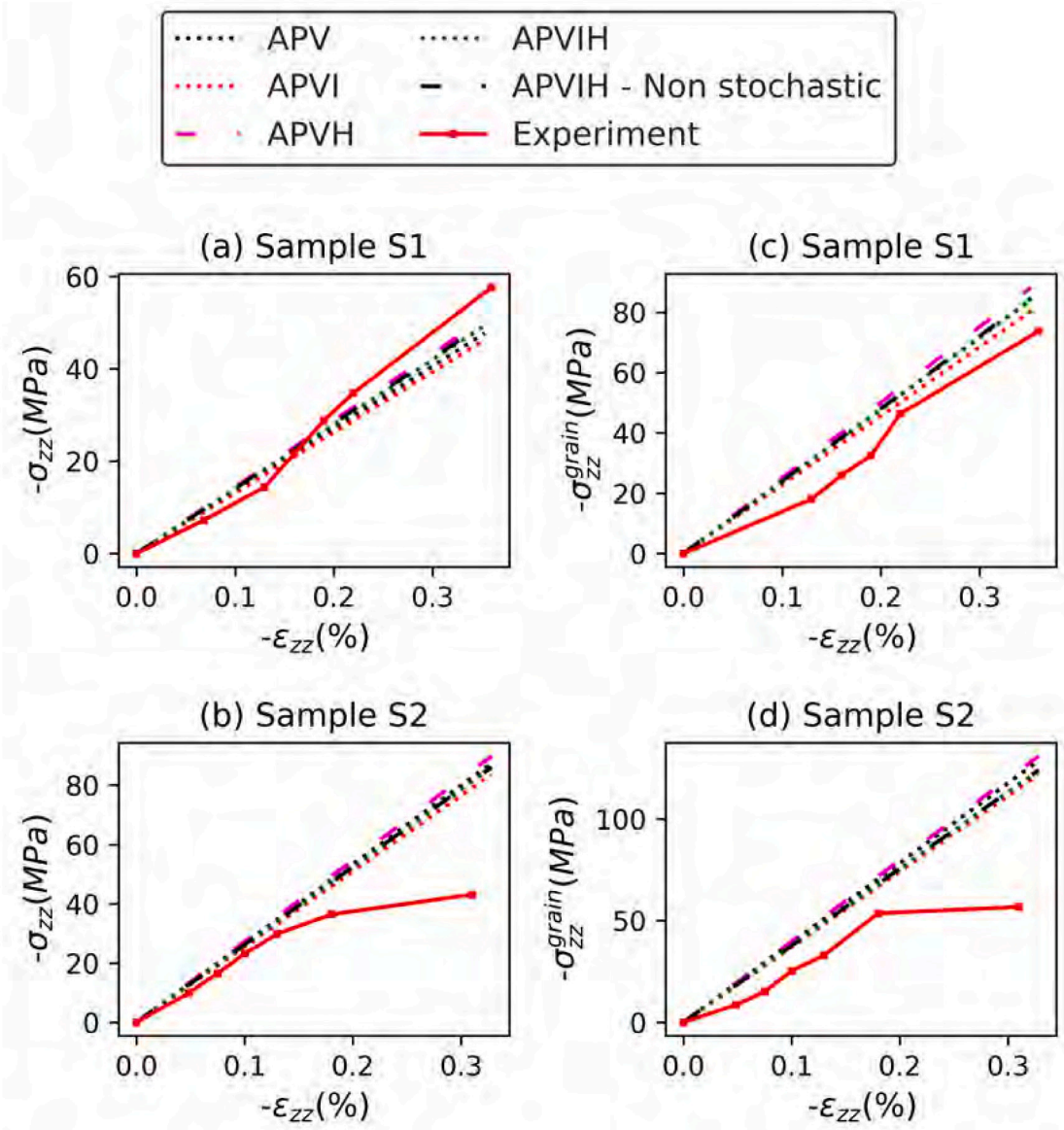

Fig. 6. Macroscale response from experiments and mesoscale simulations for samples S1 and S2. (a) Average stress–strain response in loading direction for sample S1. (b) Average stress–strain response in loading direction for sample S2. (c) Average grain stress-sample strain response in loading direction for sample S1. (d) Average grain stress-sample strain response in loading direction for sample S2.

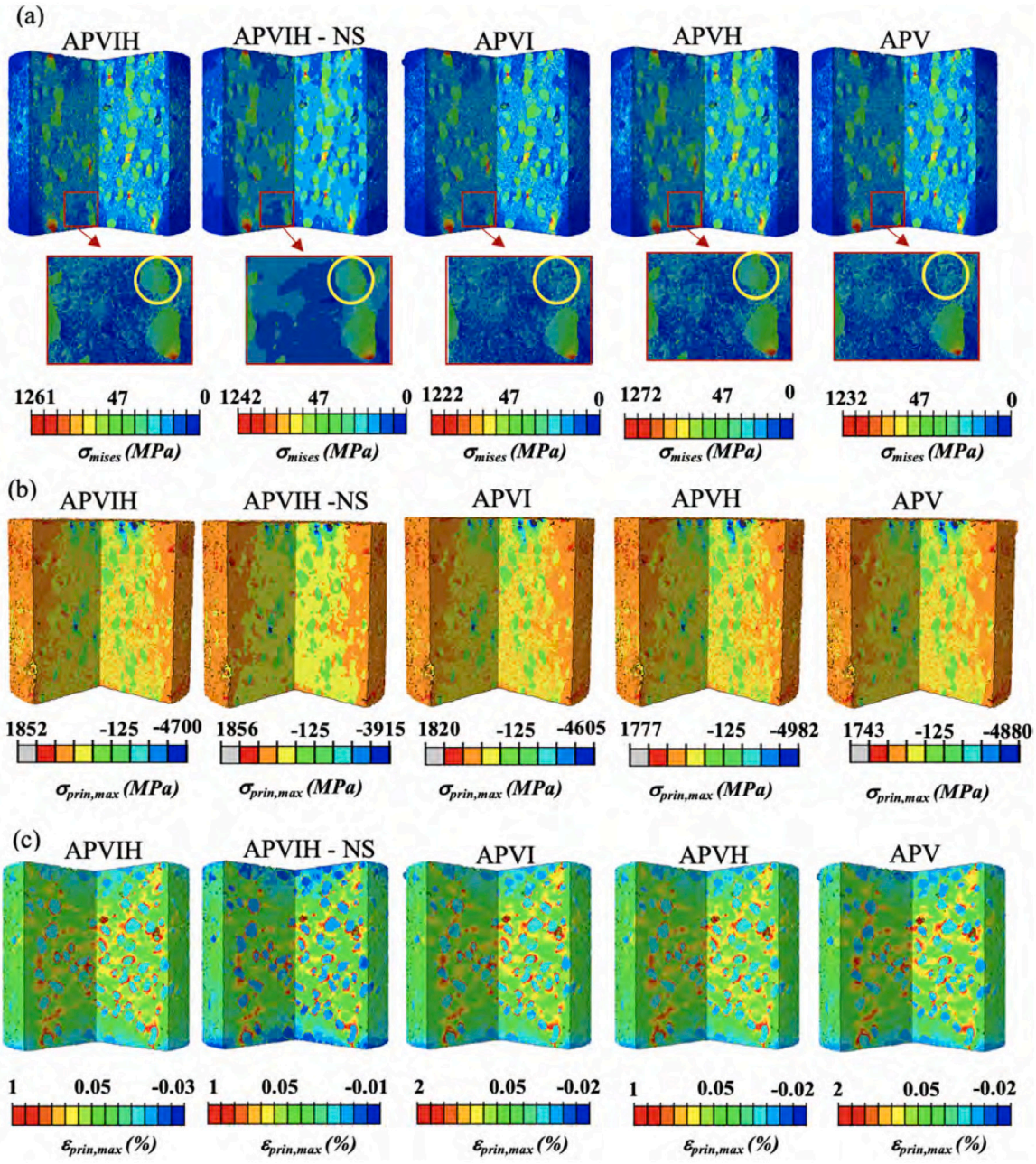

Fig. 7. (a) Contours of von-Mises stress for different levels of heterogeneities in sample S1. (b) Contours of maximum principal stress for different levels of heterogeneities in sample S1. (c) Contours of maximum principal strain for different levels of heterogeneities in sample S1. (For interpretation of the references to color in this figure legend, the reader is referred to the web version of this article.)

The reference value of the modulus of elasticity (E_{ref}) in Table 3 is the value of the modulus of elasticity corresponding to the APVIH level of heterogeneity. It can be observed that the maximum change in modulus of elasticity for sample S1 and sample S2 was approximately equal to 6% and 5%, respectively. Furthermore, the stochastic description of material properties does not result in an appreciable change in the modulus of elasticity.

Next, we explore the reason for the minimal influence of heterogeneities at the micron scale on the average stress–strain response. For this purpose, we use Mori–Tanaka's homogenization scheme to predict the average modulus of elasticity for different levels of heterogeneities considered in this study. Mori–Tanaka's approximation has been widely used to predict the homogenized stiffness of composite materials [48,49]. For $n+1$ distinct phases, Mori–Tanaka's homogenization method estimates the homogenized linear elastic, isotropic stiffness tensor according to

$$\overline{C} = \left(\sum_{\alpha=0}^{n} f_\alpha C_\alpha : \boldsymbol{A}_\alpha\right) : \left(\sum_{\alpha=0}^{n} f_\alpha \boldsymbol{A}_\alpha\right)^{-1}, \tag{4}$$

where f_α, C_α and $\boldsymbol{A}_\alpha$ represent volume fraction, the linear elastic isotropic stiffness tensor, and the strain concentration tensor of phase α, respectively. The details of the Mori–Tanaka approximation are avoided here for brevity and the reader is referred to the seminal textbooks on micromechanics for detailed explanations [50,51].

Table 4 shows the predicted modulus of elasticity from Mori–Tanaka's approximation for sample S1 and sample S2 for different levels of heterogeneities. The material properties and volume fraction of different phases used in Eq. (4) for homogenized stiffness prediction were the same as what we used in mesoscale simulations. It is interesting to observe that Mori–Tanaka's approximation predicts the modulus

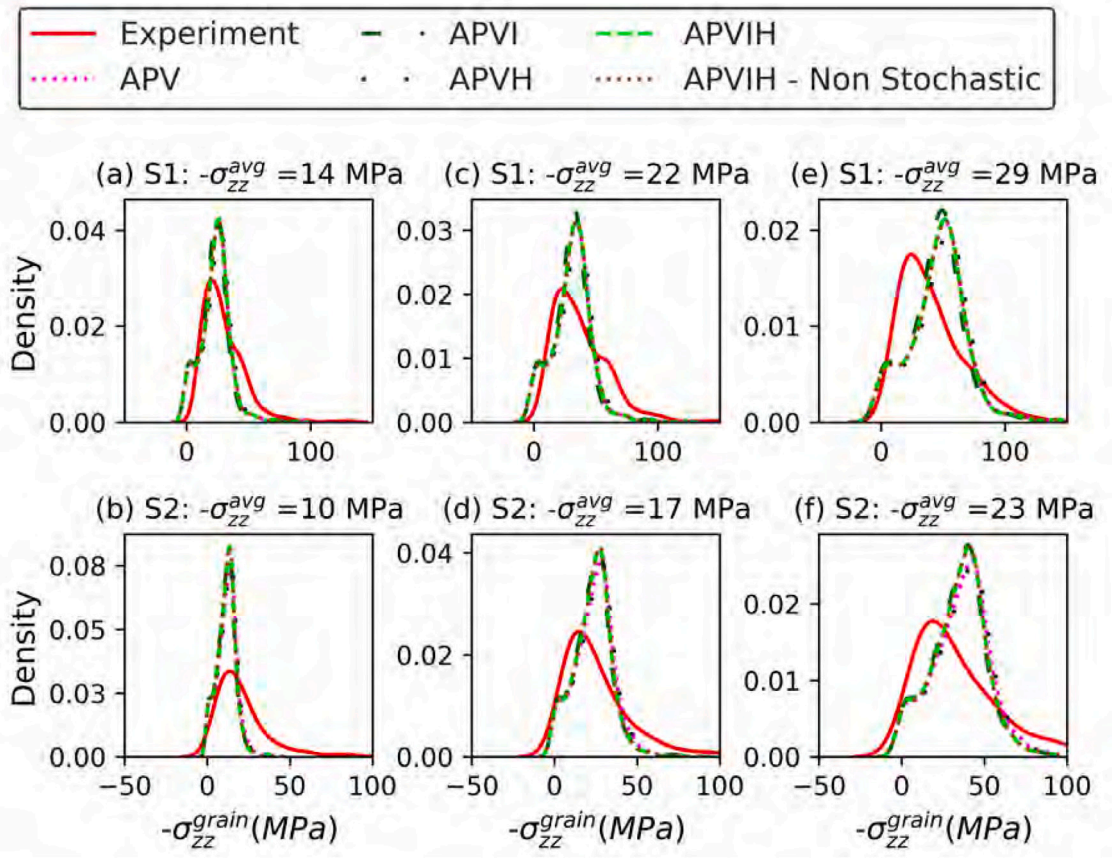

Fig. 8. Microscale response — distribution of stresses in grains in loading direction for different levels of heterogeneities in samples S1 and S2. (a), (c), (e): Sample S1 with macroscopic stress in loading direction equal to −14 MPa, −22 MPa, and −29 MPa, respectively. (b), (d), (f): Sample S2 with macroscopic stress in loading direction equal to −10 MPa, −17 MPa and −23 MPa, respectively.

Table 3
Modulus of Elasticity for different levels of heterogeneities from mesoscale simulations.

Sample/Heterogeneity	APVIH	APVIH-NS	APVI	APVH	APV
Sample S1: E(GPa)	13.99	14.12	13.10	14.41	13.52
Sample S1: $[\Delta E/E_{ref}] \times 100$	0.00	0.93	−6.36	3.00	−3.36
Sample S2: E(GPa)	26.03	26.27	25.46	27.38	26.69
Sample S2: $[\Delta E/E_{ref}] \times 100$	0.00	0.92	−2.19	5.19	2.54

Table 4
Modulus of Elasticity for different levels of heterogeneities from Mori–Tanaka approximations.

Sample/Heterogeneity	APVIH	APVIH-NS	APVI	APVH	APV
Sample S1: E(GPa)	15.44	15.44	13.30	15.81	13.62
Sample S1: $[\Delta E/E_{ref}] \times 100$	0.00	0.00	−13.86	2.40	−11.79
Sample S2: E(GPa)	26.22	26.22	24.62	27.06	25.41
Sample S2: $[\Delta E/E_{ref}] \times 100$	0.00	0.00	−6.10	3.20	−3.09

of elasticity reasonably similar to predictions from mesoscale simulations as observed in Tables 3 and 4. The influence of different levels of heterogeneities from Mori–Tanaka's approximation is also negligible as observed in Table 4. Therefore, from a practical standpoint, one can conclude that the influence of phases/heterogeneities with small phase volume fractions compared to other phases is only localized and has a negligible impact on the average stress–strain response in the elastic regime.

3.2. Microscale response

Qualitatively, the influence of heterogeneity on local stress and strain response is presented in Fig. 7, which shows contour plots of von-Mises stress, maximum principal stress, and maximum principal strain for Sample S1. The same plot for Sample S2 is not presented here for the sake of brevity. We chose von-Mises stress, maximum principal stress, and maximum principal strain in Fig. 7 as these quantities or their work conjugates are involved, either separately or together, in the onset of failure in concrete and other similar materials. It can be observed that stochastic and non-stochastic descriptions of material properties generate diffuse and smooth von-Mises stress and maximum principal stress distributions, respectively (see APVIH and APVIH-NS in Fig. 7(a) and Fig. 7(b)). The presence of a high-density phase influences the concentration of von-Mises stress. This is evident in zoomed-in regions in Fig. 7(a) in which the region marked by yellow circles shows the presence of stress concentration in heterogeneity levels APVIH, APVIH-NS, and APVIH; this stress concentration is absent in heterogeneity levels APV and APVI. The maximum principal stress contours in Fig. 7(b) also indicate concentration for different levels of heterogeneities. The maximum principal strain contours in Fig. 7(c) show concentration for all the levels of heterogeneity. The strain concentration is mostly concentrated around the aggregates in the matrix region, irrespective of the heterogeneity level incorporating or not incorporating ITZ

To elucidate the role of heterogeneity on microscale response, we investigate stresses in individual grains from mesoscale simulations and experiments employing in-situ 3DXRD measurements. We also probe the distribution of strains from mesoscale simulations in the individual phases of the matrix and matrix as a whole to illustrate the dependency

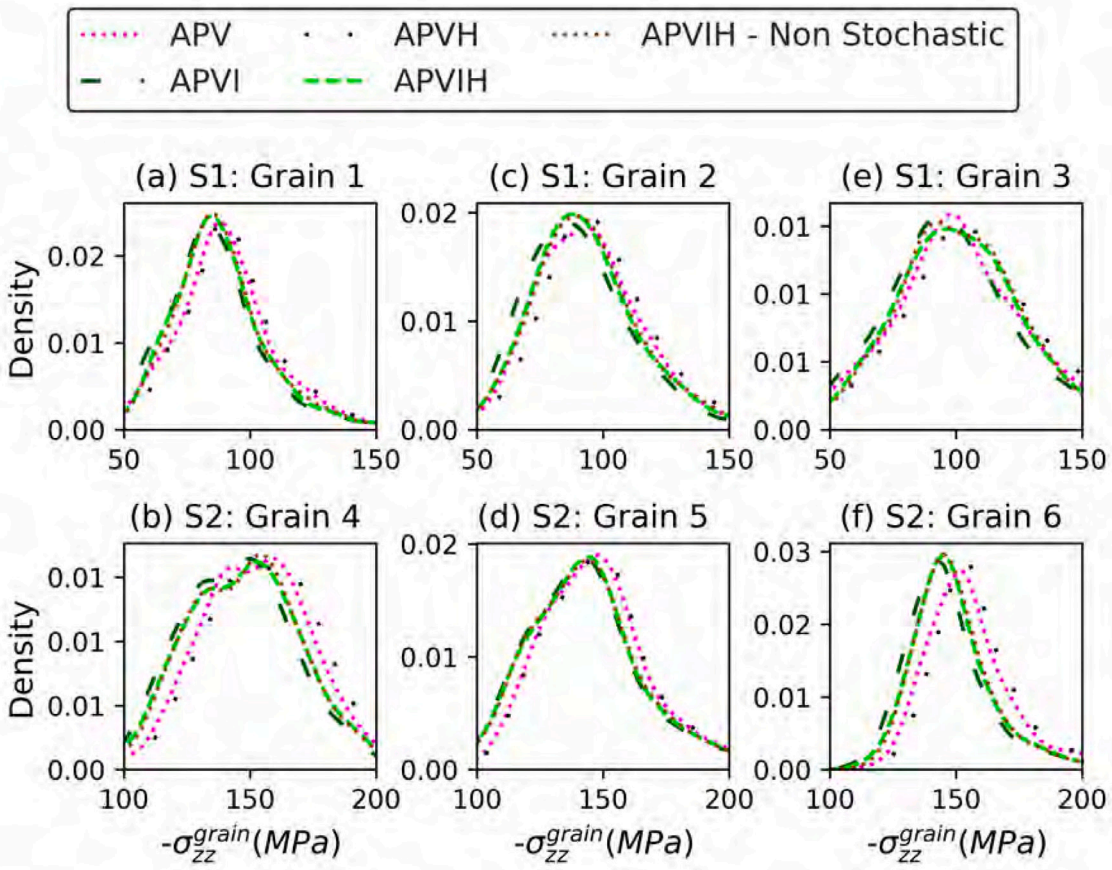

Fig. 9. Distribution of stresses in loading direction in selected individual grains for different levels of heterogeneities in samples S1 and S2. (a) Grain 1 of sample S1. (b) Grain 4 of sample S2. (c) Grain 2 of sample S1. (d) Grain 5 of sample S2. (e) Grain 3 of sample S1. (f) Grain 6 of sample S2. Note: Grains were selected randomly and were numbered only for convenience.

of local strains on different levels of heterogeneities. The local stresses in the grain phase and local strains in matrix phases are explored as a function of heterogeneity in Sections 3.2.1 and 3.2.2, respectively

3.2.1. Stresses in individual grains

Fig. 8 presents the distribution of stresses in the loading direction in individual grains in samples, S1 and S2, obtained from experiments and mesoscale simulations with different levels of heterogeneities. The stress distributions are obtained for three different macroscopic stress levels for samples S1 and S2. It can be observed that different levels of heterogeneities have a negligible influence on the distribution of stresses in individual grains. This is surprising, but nevertheless, an important result from the micromechanics perspective. Aggregate stresses relate to the tractions at the surfaces of aggregates, which in turn influence the stress state in the ITZ due to the continuity of tractions and displacements at the aggregate-ITZ interface [12,13]. The comparison of stress distribution in grains from experiments and simulations is promising. The distribution of stresses broadens with the increase in macroscopic load, and this broadening is captured in simulations as well. The broadening of stresses in grains with the increase in macroscopic load can be linked to the increase in standard deviation in grain stresses. The grains with higher stresses manifest higher tractions at the surface and are thereby expected to cause large concentration in the ITZ. A salient feature observed in Figs. 6 and 8 in terms of the mesoscale simulation accuracy is that the microscale quantities such as the distribution of grain stresses matches well with experiments but not to the same extent as an average stress–strain response. This difference in validation based on microscale and macroscale response is important for planning the validation of future mesoscale simulations in concrete and other materials. Most of the prior mesoscale simulation studies calibrated material models only based on the macroscopic stress–strain response, however, calibration based only on macroscale response does not necessarily guarantee accurate material response at the microscale. A plausible explanation for the discrepancy in grain stress distributions between experiments and simulations is the uncertainties in stress and strain measurements inferred from 3DXRD and DVC, respectively. Another possible explanation is the presence of damage or plastic deformation at matrix-grain interfaces, even in the macroscopically elastic regime, which does not occur in our elastic simulations.

Mesoscale simulations provide access to the variation in stress tensor inside the individual grains. We continue our analysis of grain stresses by investigating variation in stresses inside a few randomly selected grains that approximately lie in the central region of the sample, far from the boundary. Fig. 9 shows the distribution of stresses in the loading direction for three grains, each from samples S1 and S2, for a constant macroscopic load. It can be observed that different levels of heterogeneity result in appreciable differences in stress distribution inside the grains. For instance, looking at Fig. 9(f), it is clear that heterogeneity's 'APV' and 'APVH' produce different stress distribution inside the grain compared to the heterogeneity's 'APVI', APVIH and APVIH — Non Stochastic. Therefore, concentration in grain stresses at a length scale smaller than the size of the individual grains is influenced far more by different levels of heterogeneity compared to the grain stresses at a scale equal to the size of the individual grains.

3.2.2. Strains in matrix phase

The strain concentration in the matrix phase plays a dominant role in failure initiation and propagation in concrete. The principal strain

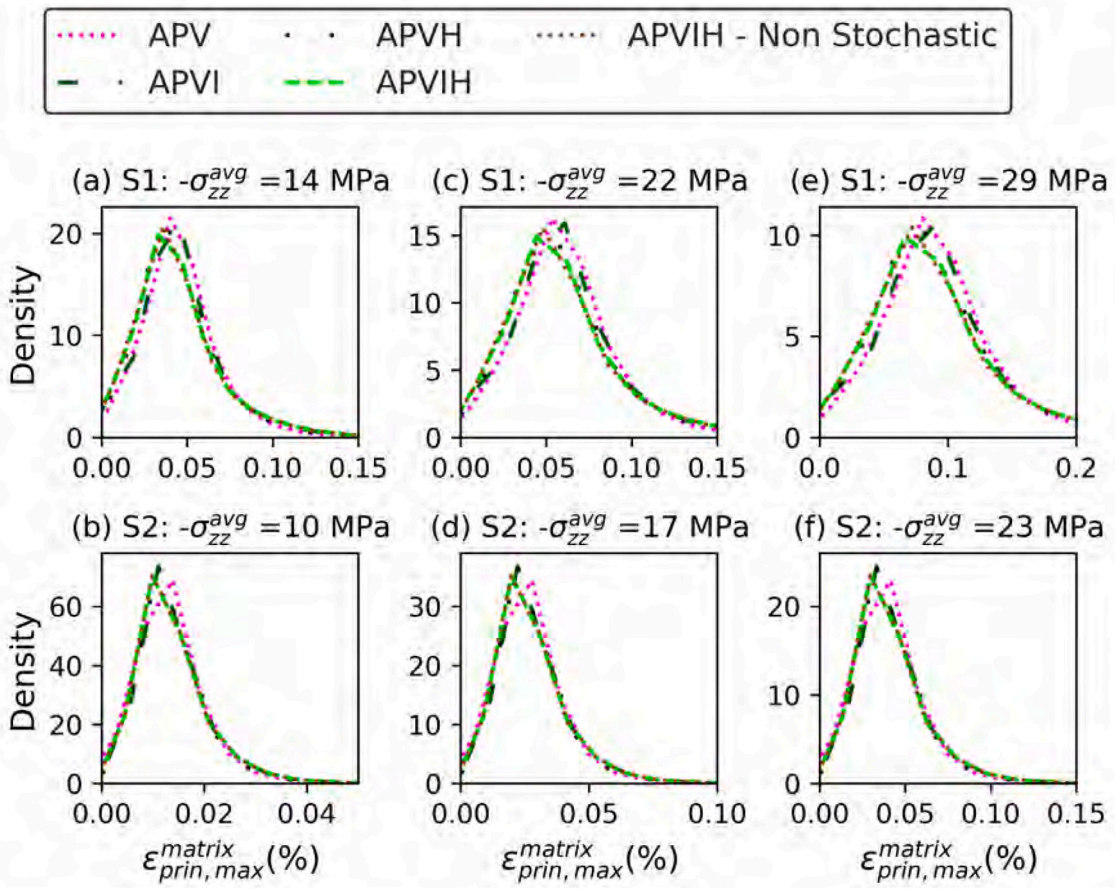

Fig. 10. Principal strain distribution in matrix phase (cement paste, ITZ, high-density phase combined) for different levels of heterogeneities in samples S1 and S2.(a), (c), (e): Sample S1 with macroscopic stress in loading direction equal to −14 MPa, −22 MPa and −29 MPa, respectively. (b), (d), (f): Sample S2 with macroscopic stress in loading direction equal to −10 MPa, −17 MPa, and −23 MPa, respectively.

distribution in the matrix phase (cement paste, ITZ, and high-density phase combined together) is shown for different levels of heterogeneity in Fig. 10. It can be observed that with the increase in the macroscopic load, the distribution of strains in the matrix phase widens, much like the widening of stresses in grains as observed in Fig. 8. In other words, the standard deviation of strains in the matrix phase increases with the increase in macroscopic load. The influence of different levels of heterogeneity on the distribution of matrix strains is noticeable but may or may not be considered significant. However, by plotting the distribution of matrix strains in Fig. 10, and not the strains in individual phases in the matrix (high-density phase, ITZ, and cement paste), the influence of heterogeneity on strain concentration is masked to a certain extent.

Next, we precisely unveil this masking effect on strain concentration by analyzing strains in individual phases in the matrix. Fig. 11 shows the distribution of principal strains in cement paste, ITZ, and high-density phase for samples S1 and S2 for heterogeneity levels APVIH, APVIH-NS, and APV. The heterogeneities APVIH and APVIH-NS include all the phases in the matrix considered in this study, therefore appropriate for investigating strains in individual phases in the matrix. The heterogeneity level APV which does not include ITZ and high-density phase is included in Fig. 11 to isolate the strain concentration effects in ITZ and high-density phase due to their spatial location from the strain concentrations due to their material properties. Let us first confine our discussion to strain concentrations in heterogeneity levels APVIH and APVIH-NS, as presented in Fig. 11(a)–(d). It can be observed that principal strain distributions in the cement phase, ITZ and high-density phase are significantly different, for both samples S1 and S2. Principal strains are maximum in ITZ, followed by cement paste and high-density phase. In addition, the standard deviation of the strains in ITZ is significantly large than the standard deviation in cement paste and high-density phase. The large standard deviation in the ITZ can be linked to the standard deviation in aggregate stresses because aggregate stresses are related to the tractions at the aggregate surfaces which influence the stress states in the ITZ. The stochastic properties of ITZ do not seem to be the cause of the large standard deviation in principal strain distribution, as is evident in Fig. 11(a)–(d).

We now compare the principal strain distribution in different phases in heterogeneity level APV, shown in Fig. 11(e) and (f), with the principal strain distributions in heterogeneity level APVIH, shown in Fig. 11(a)and (b). The APV heterogeneity level does not include ITZ and the high-density phase; the material properties of cement paste are assigned to ITZ and the high-density phase regions, but for analysis, we extract strains in the regions that are ITZ and high-density phase in XRCT microstructure. It can be observed from Fig. 11(e) and (f) that the principal strain distribution in the high-density phase and cement paste is similar for heterogeneity level APV. This is expected as the high-density phase is not included in simulations for heterogeneity level APV. However, the principal strain distribution for heterogeneity level APV, presented in Fig. 11(e)and (f), shows a larger strain variance in ITZ compared to cement paste and the high-density phase region, even though the material properties of ITZ were not included in this simulation. This naturally leads us to conclude that the strain concentration in the ITZ region for APV level heterogeneity occurs due to its location adjacent to the aggregates. This is a noteworthy observation from the mesoscale modeling perspective as concentration in a matrix adjacent to aggregates can be captured even if ITZ is not considered separately as a continuum element. This result supports the prior mesoscale simulation studies that considered ITZ as an interface element to predict

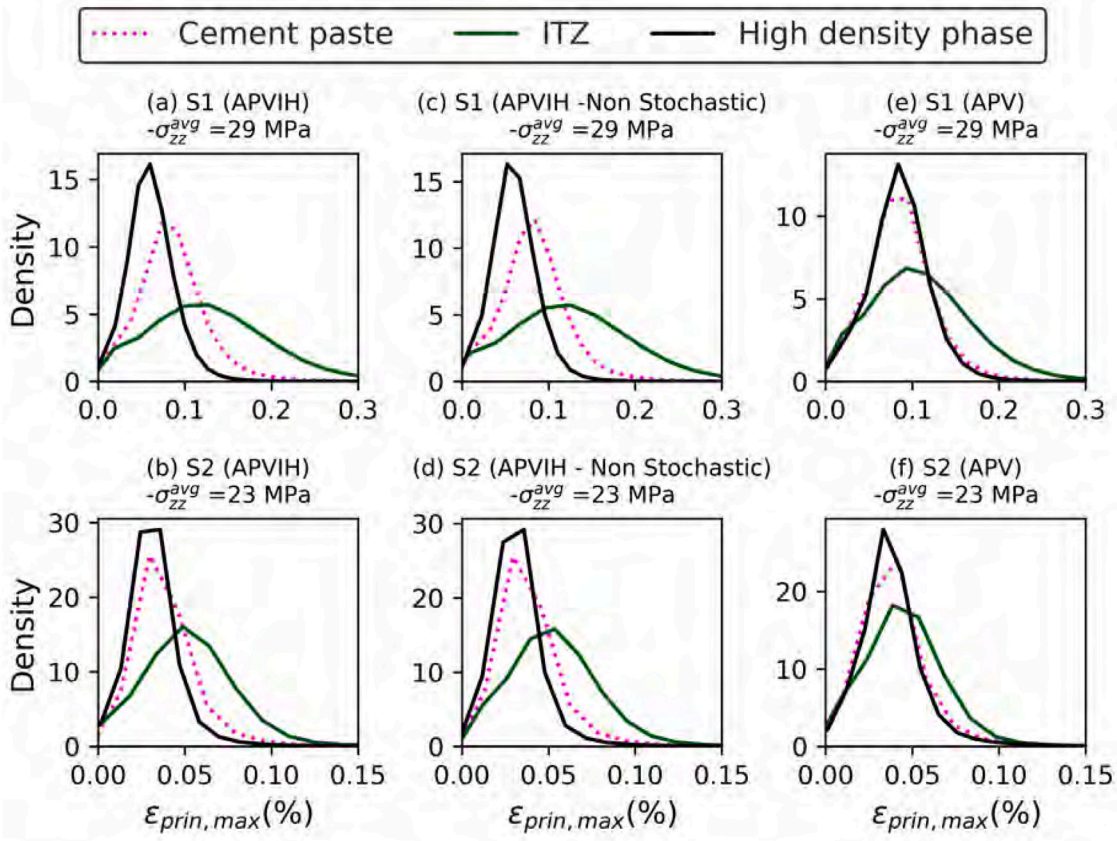

Fig. 11. Principal strain distribution in cement Paste, ITZ and high-density phase in samples S1 and S2. (a), (c), (e): Sample S1 with heterogeneity level APVIH, APVIH — Non Stochastic and APV, respectively. (b), (d), (f): Sample S2 with heterogeneity level APVIH, APVIH — Non Stochastic and APV, respectively.

failure, and not as a continuum element, for numerical convenience. However, when comparing Fig. 11(a), (b) and Fig. 11(e), (f); it is clear that the extent of the strain variance in ITZ captured in heterogeneity level APVIH is far greater compared to the strain variance captured in heterogeneity level APV. Essentially there are two components of strain concentration in ITZ: one due to their location being adjacent to aggregates and the other due to inferior material properties compared to the other regions in the matrix. Therefore, if ITZ is not included as a continuum element in mesoscale simulations, the component of strain concentration in ITZ due to the inferior material properties will not be captured. The strain variance in the high-density phase due to its location is negligible as the principal strain distribution for the high-density phase and cement paste are almost the same for APV level heterogeneity, as shown in Fig. 11(e) and (f). Therefore, the strain concentration in the high-density phase is due to the contrast in material properties with the rest of the cement paste and can only be captured by incorporating the high-density phase as heterogeneity in a mesoscale model, which is typically missing in most of the prior studies.

3.3. Representative volume element predictions

The quantitative determination of the Representative Volume Element (RVE) is discussed here for concrete samples S1 and S2. Fig. 12 shows the variograms for Sample S1 determined based on normal stresses transverse to the direction of macroscopic loading, normal stresses in the direction of macroscopic loading, principal tensile stresses, von-Mises stresses, and phase volume fractions. Fig. 13 shows the same variograms but for Sample S2. The RVE size is obtained corresponding to the value of the coefficient of the variation equal to 0.1. It can be observed from Fig. 12 that different levels of heterogeneity do not have any influence on RVE size determined based on different stress components. Fig. 12 reveals a remarkable result on RVE size prediction: the size of the RVE is significantly larger when determined based on principal stresses and normal stresses transverse to the direction of loading compared to the RVE size determined based on normal stresses in the direction of loading, von Mises stresses and phase volume fractions. The RVE sizes based on transverse normal stresses and principal tensile stresses are approximately 8 D_{max} and 7.5 D_{max}, respectively. D_{max} equal to 125 μ, is the largest size of the grain used in the concrete samples, determined based on the size of the sieve on which grains were retained. The RVE sizes based on normal stresses in the loading direction, von-Mises stresses, and phase fractions are 3.5 D_{max}, 3 D_{max}, and 2.5 D_{max}, respectively. In the case of phase volume fraction, RVE sizes predicted from grain size are critical as microstructural features in other phases are significantly smaller in size compared to the size of grain. The grain phase constrains RVE size to be at least greater than the size of the largest individual grain. RVE size equal to 2.5 D_{max} predicted based on the phase volume fraction is within the range of 2.4 D_{max} - 3.7 D_{max} suggested in [52].

We also analyzed data to predict the RVE size for Sample S2, which has a higher aggregate volume fraction and different material properties compared to Sample S1. The findings from the RVE prediction for Sample S1 were also observed in Sample S2. The principle tensile stresses and normal stresses transverse to the direction of the loading are the most crucial for RVE prediction among all the variables considered in this study. It should be noted that the RVE size predictions for Sample S1 and Sample S2 cannot be generalized for aggregate volume fractions as the material properties and void volume fractions were different for the two samples (see Fig. 13).

4. Conclusion

In this work, we studied the levels of heterogeneities that are important in mesoscale modeling of concrete with a focus on five phases:

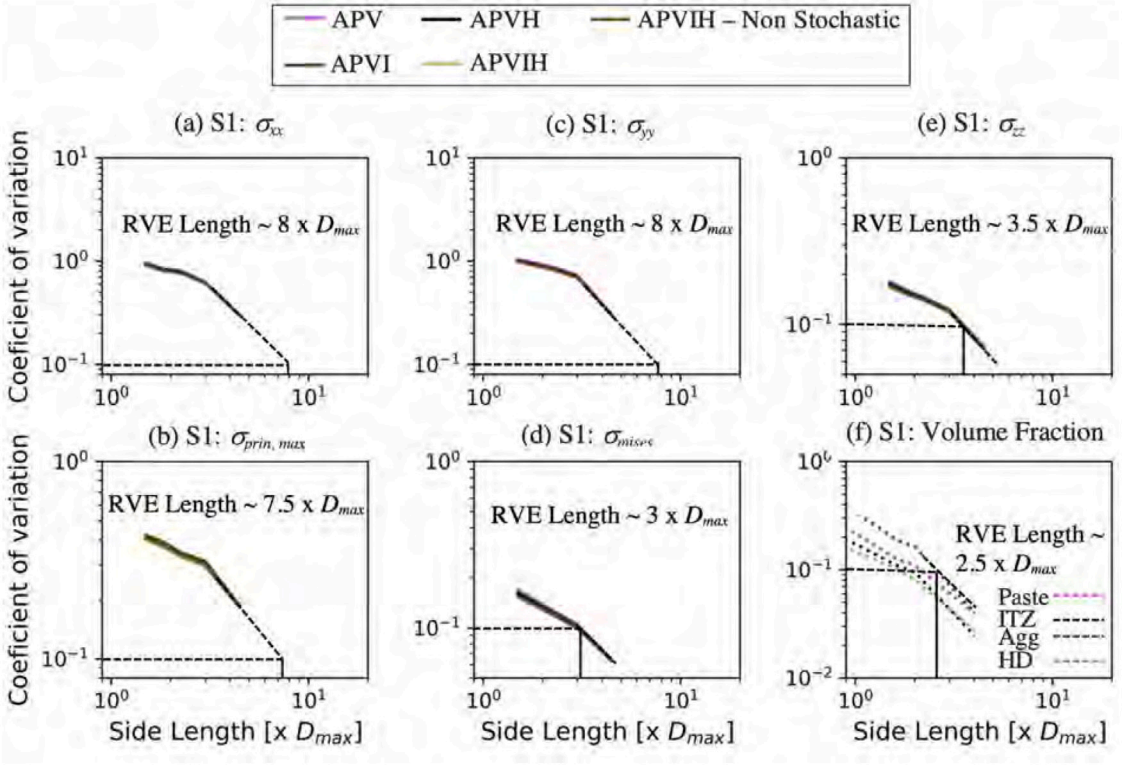

Fig. 12. RVE size prediction in sample S1 based on different quantities. (a) Normal stresses transverse to the direction of loading (σ_{xx}). (b) Maximum principal tensile stress ($\sigma_{prin,max}$). (c) Normal stresses transverse to the direction of loading (σ_{yy}). (d) von Mises stress (σ_{yy}). (e) Normal stresses in the direction of loading (σ_{zz}). (f) Phase volume fractions.

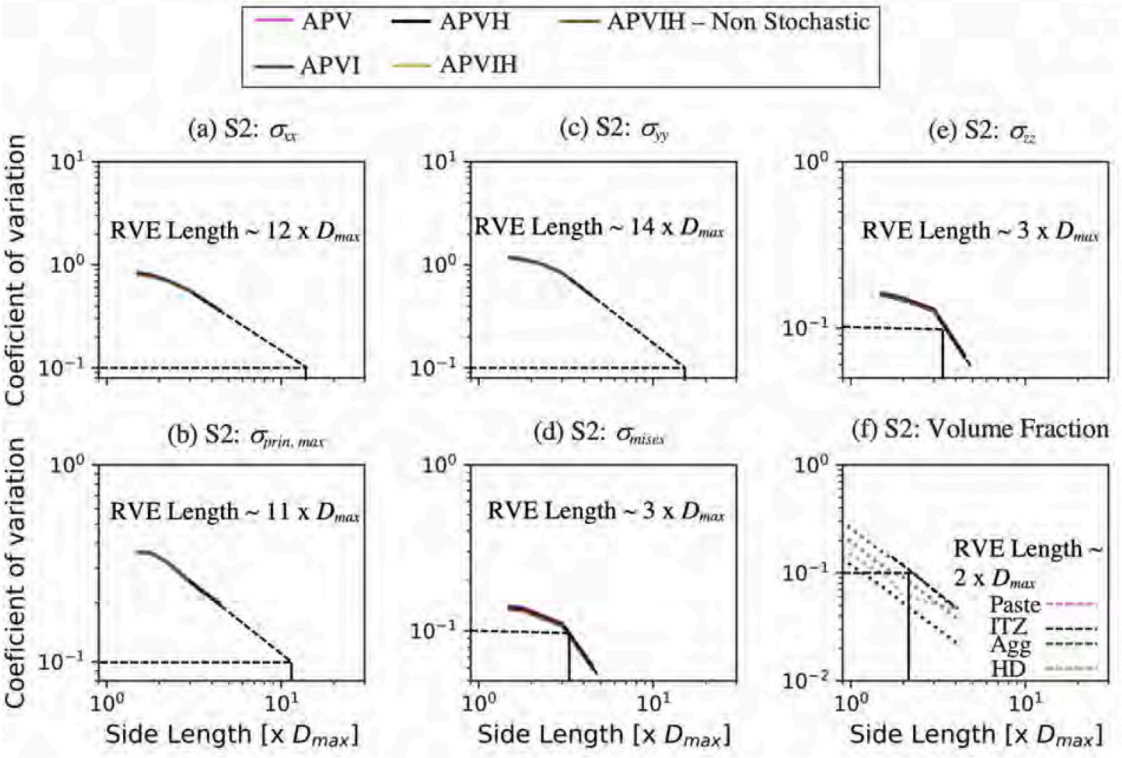

Fig. 13. RVE size prediction in sample S2 based on different quantities. (a) Normal stresses transverse to the direction of loading (σ_{xx}). (b) Maximum principal tensile stress ($\sigma_{prin,max}$). (c) Normal stresses transverse to the direction of loading (σ_{yy}). (d) von Mises stress (σ_{yy}). (e) Normal stresses in the direction of loading (σ_{zz}). (f) Phase volume fractions.

aggregates, ITZ, cement paste, high-density phase, and air voids. We brought together a suite of techniques including mesoscale modeling, XRCT imaging, and 3DXRD measurements to study the mechanics of concrete at the macro–micro scale on two samples, S1 and S2. Sample S2 had a higher aggregate volume fraction compared to sample S1. Our work leads us to interesting findings, some specific to the role of heterogeneities in concrete, others with implications for mesoscale simulation accuracy, and RVE size predictions that can be useful in general to mesoscale modeling in concrete. The key findings from our work are summarized below.

1. The average stress–strain response of the whole sample and the average stress–strain response of the grain phase from mesoscale modeling were in acceptable agreement with the experiments. The distribution of stresses in individual grains, which represents a microscale quantity, compared well between experiments and simulations but not to the same extent as observed in the average stress–strain response. This outcome is powerful for future mesoscale simulations in concrete, suggesting the need to validate modeling with experiments at both the macroscale and microscale.
2. The average stress–strain response was marginally affected by different levels of heterogeneities which consisted of only small phase volume fractions compared to the aggregate volume fraction and cement paste volume fraction. The average elastic modulus in the loading direction differed by no more than 6.36% and 5.19% for different levels of the heterogeneities in Samples S1 and S2, respectively. A similar observation was concluded from Mori–Tanaka's prediction for elastic modulus for different levels of heterogeneities. Therefore, for the purpose of predicting average elastic modulus, ignoring heterogeneities corresponding to phases with small volume fractions may be reasonable if an error within 10% is acceptable. In such cases, considering concrete as two-phase or three-phase material would be appropriate, as is done in most of the prior work.
3. The distribution of strains in cement paste, ITZ, and high-density phases differed significantly. The strains in ITZ experienced maximum concentration and standard deviation. The strain concentration in ITZ had two components: one due to the location of ITZ being adjacent to aggregates and the other due to inferior material properties of ITZ. Both components were significant, however, the second component is often ignored in mesoscale simulations by considering ITZ as an interface element and not as a continuum element. We suggest considering ITZ as an interface element might be a reasonable approximation if computational cost is a constraint because a significant amount of concentration due to the location of ITZ would still be captured. However, the high-density phase had only one component of strain concentration, due to its contrast in material properties with cement paste, and not due to its location. Therefore, the high-density phase should be considered explicitly in mesoscale modeling to capture its concentration effect on strains in the matrix.
4. The grain stresses were influenced to some extent by the presence of heterogeneity at a scale smaller than the size of the individual grains. At larger scales, there was a negligible effect on grain stresses for different levels of heterogeneities
5. RVE sizes predicted based on principal tensile stresses and normal stresses transverse to the direction of loading were significantly larger compared to RVE sizes predicted based on von-Mises stresses, normal stresses in the direction of loading, and phase volume fractions. Overall, RVE sizes between $7.5\,D_{max}$ and $11\,D_{max}$ may be considered appropriate for principal tensile stresses based on our findings from Samples S1 and S2. RVE size findings for Sample S1 and Sample S2 should not be generalized for the effect of aggregate volume fractions as the material properties were different for the two samples. More work is needed to predict the RVE sizes as the aggregate volume fraction changes.

CRediT authorship contribution statement

Mohmad M. Thakur: Conceptualization, Methodology, Software, Formal analysis, Writing – original draft. **N. Axel Henningsson:** Investigation. **Jonas Engqvist:** Investigation, Resources. **Pierre-Olivier Autran:** Investigation, Formal analysis. **Jonathan P. Wright:** Formal analysis. **Ryan C. Hurley:** Conceptualization, Methodology, Formal analysis, Resources, Writing – review & editing, Project administration, Funding acquisition.

Declaration of competing interest

The authors declare that they have no known competing financial interests or personal relationships that could have appeared to influence the work reported in this paper.

Data availability

Data will be made available on request.

Acknowledgments

MMT and RCH acknowledge support by the U.S. National Science Foundation Award No. CMMI-2125023. All authors acknowledge support from ESRF, France for synchrotron beamtime under proposal numbers ma-4978.

References

[1] S. Diamond, The microstructure of cement paste and concrete - A visual primer, Cem. Concr. Compos. 26 (8) (2004) 919–933, http://dx.doi.org/10.1016/j.cemconcomp.2004.02.028.
[2] Z. Yang, W. Ren, R. Sharma, S. McDonald, M. Mostafavi, Y. Vertyagina, T.J. Marrow, In-situ X-ray computed tomography characterisation of 3D fracture evolution and image-based numerical homogenisation of concrete, Cem. Concr. Compos. 75 (2017) 74–83, http://dx.doi.org/10.1016/j.cemconcomp.2016.10.001, URL http://dx.doi.org/10.1016/j.cemconcomp.2016.10.001.
[3] F.J. Ulm, M. Vandamme, C. Bobko, J. Alberto Ortega, K. Tai, C. Ortiz, Statistical indentation techniques for hydrated nanocomposites: Concrete, bone, and shale, J. Am. Ceram. Soc. 90 (9) (2007) 2677–2692, http://dx.doi.org/10.1111/j.1551-2916.2007.02012.x.
[4] C. Hu, Z. Li, A review on the mechanical properties of cement-based materials measured by nanoindentation, Constr. Build. Mater. 90 (2015) 80–90, http://dx.doi.org/10.1016/j.conbuildmat.2015.05.008.
[5] G. Constantinides, F.J. Ulm, K. Van Vliet, On the use of nanoindentation for cementitious materials, Mater. Struct./Mater. Construct. 36 (257) (2003) 191–196, http://dx.doi.org/10.1617/14020.
[6] G. Constantinides, F.-J. Ulm, The effect of two types of CSH on the elasticity of cement-based materials: Results from nanoindentation and micromechanical modeling, Cem. Concr. Res. 34 (1) (2004) 67–80.
[7] M. Sebastiani, R. Moscatelli, F. Ridi, P. Baglioni, F. Carassiti, High-resolution high-speed nanoindentation mapping of cement pastes: Unravelling the effect of microstructure on the mechanical properties of hydrated phases, Mater. Des. 97 (2016) 372–380, http://dx.doi.org/10.1016/j.matdes.2016.02.087.
[8] X. Chen, D. Hou, Y. Han, X. Ding, P. Hua, Clustering analysis of grid nanoindentation data for cementitious materials, J. Mater. Sci. 56 (21) (2021) 12238–12255, http://dx.doi.org/10.1007/s10853-021-05848-8.
[9] J.J. Hughes, P. Trtik, Micro-mechanical properties of cement paste measured by depth-sensing nanoindentation: A preliminary correlation of physical properties with phase type, Mater. Charact. 53 (2–4) (2004) 223–231, http://dx.doi.org/10.1016/j.matchar.2004.08.014.
[10] W. Wilson, L. Sorelli, A. Tagnit-Hamou, Automated coupling of NanoIndentation and Quantitative Energy-Dispersive Spectroscopy (NI-QEDS): A comprehensive method to disclose the micro-chemo-mechanical properties of cement pastes, Cem. Concr. Res. 103 (August 2017) (2018) 49–65, http://dx.doi.org/10.1016/j.cemconres.2017.08.016.
[11] P. Mondal, S.P. Shah, L.D. Marks, Nanoscale characterization of cementitious materials, ACI Mater. J. 105 (2) (2008) 174.
[12] M. Königsberger, B. Pichler, C. Hellmich, Micromechanics of ITZ-aggregate interaction in concrete part I: Stress concentration, J. Am. Ceram. Soc. 97 (2) (2014) 535–542, http://dx.doi.org/10.1111/jace.12591.
[13] M. Königsberger, B. Pichler, C. Hellmich, Micromechanics of ITZ-aggregate interaction in concrete part II: Strength upscaling, J. Am. Ceram. Soc. 97 (2) (2014) 543–551.

[14] M. Königsberger, M. Hlobil, B. Delsaute, S. Staquet, C. Hellmich, B. Pichler, Hydrate failure in ITZ governs concrete strength: A micro-to-macro validated engineering mechanics model, Cem. Concr. Res. 103 (November 2017) (2018) 77–94, http://dx.doi.org/10.1016/j.cemconres.2017.10.002.

[15] M.A. Homel, J. Iyer, S.J. Semnani, E.B. Herbold, Cement and Concrete Research Mesoscale model and X-ray computed micro-tomographic imaging of damage progression in ultra-high-performance concrete, Cem. Concr. Res. 157 (October 2021) (2022) 106799, http://dx.doi.org/10.1016/j.cemconres.2022.106799.

[16] Y. Gao, W. Li, K. Wu, Q. Yuan, Modeling the elastic modulus of cement paste with X-ray computed tomography and a hybrid analytical-numerical algorithm: The effect of structural heterogeneity, Cem. Concr. Compos. 122 (January) (2021) http://dx.doi.org/10.1016/j.cemconcomp.2021.104145.

[17] Ł. Skarżyński, J. Tejchman, Experimental investigations of fracture process in concrete by means of X-ray micro-computed tomography, Strain 52 (1) (2016) 26–45.

[18] S. Häfner, S. Eckardt, T. Luther, C. Könke, Mesoscale modeling of concrete: Geometry and numerics, Comput. Struct. 84 (7) (2006) 450–461.

[19] M. Nitka, J. Tejchman, A three-dimensional meso-scale approach to concrete fracture based on combined DEM with X-ray μCT images, Cem. Concr. Res. 107 (2018) 11–29.

[20] S.M. Kim, R.K. Abu Al-Rub, Meso-scale computational modeling of the plastic-damage response of cementitious composites, Cem. Concr. Res. 41 (3) (2011) 339–358, http://dx.doi.org/10.1016/j.cemconres.2010.12.002.

[21] J.S. Kim, S.Y. Chung, D. Stephan, T.S. Han, Issues on characterization of cement paste microstructures from μ-CT and virtual experiment framework for evaluating mechanical properties, Constr. Build. Mater. 202 (2019) 82–102, http://dx.doi.org/10.1016/j.conbuildmat.2019.01.030.

[22] G. Constantinides, F.J. Ulm, The nanogranular nature of C-S-H, J. Mech. Phys. Solids 55 (1) (2007) 64–90, http://dx.doi.org/10.1016/j.jmps.2006.06.003.

[23] P.D. Tennis, H.M. Jennings, Model for two types of calcium silicate hydrate in the microstructure of Portland cement pastes, Cem. Concr. Res. 30 (6) (2000) 855–863, http://dx.doi.org/10.1016/S0008-8846(00)00257-X.

[24] P. Wriggers, S.O. Moftah, Mesoscale models for concrete: Homogenisation and damage behaviour, Finite Elem. Anal. Des. 42 (7 SPEC. ISS.) (2006) 623–636, http://dx.doi.org/10.1016/j.finel.2005.11.008.

[25] D. Wei, R.C. Hurley, L.H. Poh, D. Dias-da Costa, Y. Gan, The role of particle morphology on concrete fracture behaviour: A meso-scale modelling approach, Cem. Concr. Res. 134 (February) (2020) http://dx.doi.org/10.1016/j.cemconres.2020.106096.

[26] W. Trawiński, J. Tejchman, J. Bobiński, A three-dimensional meso-scale modelling of concrete fracture, based on cohesive elements and X-ray μCT images, Eng. Fract. Mech. 189 (2018) 27–50, http://dx.doi.org/10.1016/j.engfracmech.2017.10.003.

[27] R. Hurley, S. Hall, J. Andrade, J. Wright, Quantifying interparticle forces and heterogeneity in 3D granular materials, Phys. Rev. Lett. 117 (9) (2016) 098005.

[28] N. Viganò, P. Cloetens, M. Di Michiel, A. Rack, P. Tafforeau, Redefining the ESRF tomography software, in: Digital Holography and Three-Dimensional Imaging, Optica Publishing Group, 2021, pp. DF2G–4.

[29] J. Wright, Imaged11, 2020, Available at https://Github.Com/FABLE-3DXRD/ImageD11.

[30] J. Oddershede, S. Schmidt, H.F. Poulsen, H.O. Sørensen, J. Wright, W. Reimers, Determining grain resolved stresses in polycrystalline materials using three-dimensional X-ray diffraction, J. Appl. Crystallogr. 43 (3) (2010) 539–549.

[31] R. Hurley, J. Lind, D. Pagan, M. Akin, E. Herbold, In situ grain fracture mechanics during uniaxial compaction of granular solids, J. Mech. Phys. Solids 112 (2018) 273–290.

[32] P. Heyliger, H. Ledbetter, S. Kim, Elastic constants of natural quartz, J. Acoust. Soc. Am. 114 (2) (2003) 644–650.

[33] O. Stamati, E. Andò, E. Roubin, R. Cailletaud, M. Wiebicke, G. Pinzon, C. Cyrille, R. Hurley, R. Caulk, D. Caillerie, et al., Spam: software for practical analysis of materials, J. Open Source Softw. 5 (51) (2020) 2286.

[34] B.D. Lucas, T. Kanade, An iterative image registration technique with an application to stereo vision, in: Proceedings of the International Joint Conference on Artificial Intelligence, Vancouver, British Columbia, 1981, pp. 674–679.

[35] M.A. Sutton, J.J. Orteu, H. Schreier, Image Correlation for Shape, Motion and Deformation Measurements: Basic Concepts, Theory and Applications, Springer Science & Business Media, 2009.

[36] G. Gerig, O. Kubler, R. Kikinis, F.A. Jolesz, Nonlinear anisotropic filtering of MRI data, IEEE Trans. Med. Imaging 11 (2) (1992) 221–232.

[37] O. Stamati, E. Roubin, E. Andò, Y. Malecot, Phase segmentation of concrete x-ray tomographic images at meso-scale: Validation with neutron tomography, Cem. Concr. Compos. 88 (2018) 8–16, http://dx.doi.org/10.1016/j.cemconcomp.2017.12.011.

[38] R. Hurley, D. Pagan, An in-situ study of stress evolution and fracture growth during compression of concrete, Int. J. Solids Struct. 168 (2019) 26–40.

[39] S.C. Mayo, T.J. Davis, T.E. Gureyev, P.R. Miller, D. Paganin, A. Pogany, A.W. Stevenson, S. Wilkins, X-ray phase-contrast microscopy and microtomography, Opt. Express 11 (19) (2003) 2289–2302.

[40] K.L. Scrivener, A.K. Crumbie, P. Laugesen, The interfacial transition zone (ITZ) between cement paste and aggregate in concrete, Interface Sci. 12 (4) (2004) 411–421.

[41] X. Chen, T. Sun, T. Sun, H. Yin, D. Hou, Multiscale Modeling of Elastic Modulus across Micro-Meso-Macroscales Based on Grid-Nanoindentation Test for Cementitious Materials, J. Mater. Civ. Eng. 34 (7) (2022) 1–10, http://dx.doi.org/10.1061/(asce)mt.1943-5533.0004267.

[42] S.-W. Cho, C.-C. Yang, R. Huang, Effect of aggregate volume fraction on the elastic moduli and void ratio of cement-based, J. Mar. Sci. Technol. 8 (1) (2000) 1.

[43] T. Kanit, S. Forest, I. Galliet, V. Mounoury, D. Jeulin, Determination of the size of the representative volume element for random composites: Statistical and numerical approach, Int. J. Solids Struct. 40 (13–14) (2003) 3647–3679, http://dx.doi.org/10.1016/S0020-7683(03)00143-4.

[44] W.J. Drugan, J.R. Willis, A micromechanics-based nonlocal constitutive equation and estimates of representative volume element size for elastic composites, J. Mech. Phys. Solids 44 (4) (1996) 497–524, http://dx.doi.org/10.1016/0022-5096(96)00007-5.

[45] M. Schneider, M. Josien, F. Otto, Representative volume elements for matrix-inclusion composites - a computational study on the effects of an improper treatment of particles intersecting the boundary and the benefits of periodizing the ensemble, J. Mech. Phys. Solids 158 (March 2021) (2022) 104652, http://dx.doi.org/10.1016/j.jmps.2021.104652.

[46] C. Lantuejoul, Ergodicity and integral range, J. Microsc. 161 (3) (1991) 387–403.

[47] G. Shahin, E.B. Herbold, S.A. Hall, R.C. Hurley, Quantifying the hierarchy of structural and mechanical length scales in granular systems, Extreme Mech. Lett. 51 (2022) 101590.

[48] C.-C. Yang, R. Huang, Double inclusion model for approximate elastic moduli of concrete material, Cem. Concr. Res. 26 (1) (1996) 83–91.

[49] I.C. Mihai, A.D. Jefferson, A material model for cementitious composite materials with an exterior point Eshelby microcrack initiation criterion, Int. J. Solids Struct. 48 (24) (2011) 3312–3325, http://dx.doi.org/10.1016/j.ijsolstr.2011.08.001.

[50] S. Li, G. Wang, Introduction To Micromechanics and Nanomechanics, World Scientific Publishing Company, 2008.

[51] S. Nemat-Nasser, M. Hori, Micromechanics: Overall Properties of Heterogeneous Materials, Elsevier, 2013.

[52] S.K. Sebsadji, K. Chouicha, Determining periodic representative volumes of concrete mixtures based on the fractal analysis, Int. J. Solids Struct. 49 (21) (2012) 2941–2950, http://dx.doi.org/10.1016/j.ijsolstr.2012.05.017.